Analysis and Verification of Jitter in Bang-Bang Clock and Data Recovery Circuit With a Second-Order Loop Filter

Xinyi Ge, Yong Chen, *Member, IEEE*, Xiaoteng Zhao, *Student Member, IEEE*, Pui-In Mak, *Fellow, IEEE*, and Rui P. Martins, *Fellow, IEEE*

***Abstract*— This paper provides an in-depth analysis of the third-order bang-bang clock and data recovery (BBCDR) circuit, which accurately predicts its operating characteristics, namely, the jitter transfer function (JTF), the jitter tolerance (JTOL), and the jitter generation (JGEN). By formulating the time-domain waveforms, we introduce a characterizing method and also derive the closed-form equations and their simplified versions under specific conditions, which are related with the second-order loop filter (LF). Our framework is consistent with the conclusions of the prior works. Also, we discuss through the time-domain behavior, the sinking area of the JTOL and other specific phenomenon appearing in the third-order BBCDR loop. We verify all above prediction by system-level simulations with the MATLAB/simulink model.**

***Index Terms*— Bang-bang clock and data recovery (BBCDR), bang-bang phase detector (BBPD), binary, Fourier series, jitter generation (JGEN), jitter tolerance (JTOL), jitter transfer function (JTF), linear phase detector, loop filter (LF), sinking area.**

I. Introduction

CLOCK and data recovery (CDR) circuits [1]–[6] recently incorporating a bang-bang phase detector (BBPD) are widespread in multigigabit data links, e.g., backplane and optical communications. Compared with its linear counterparts [7]–[10], the BBPD has several advantages of design simplicity, proper phase adjustment, all-digital integration [11]–[15], and high-frequency operation [16].

Manuscript received January 21, 2019; revised April 14, 2019; accepted May 3, 2019. Date of publication June 6, 2019; date of current version September 25, 2019. This work was supported in part by the University of Macau under Grant MYRG2017-00167-AMSV and in part by Macau Science and Technology Development Fund (FDCT)—SKL Fund. *(Corresponding author: Yong Chen.)*

X. Ge, Y. Chen, and X. Zhao are with the State-Key Laboratory of Analog and Mixed-Signal VLSI, University of Macau, Macau 999078, China (e-mail: ychen@um.edu.mo).

P.-I. Mak is with the State-Key Laboratory of Analog and Mixed-Signal VLSI, University of Macau, Macau 999078, China, and also with the Department of Electrical and Computer Engineering, Faculty of Science and Technology, University of Macau, Macau 999078, China (e-mail: pimak@um.edu.mo).

R. P. Martins is with the State-Key Laboratory of Analog and Mixed-Signal VLSI, University of Macau, Macau 999078, China, and also with the Department of Electrical and Computer Engineering, Faculty of Science and Technology, University of Macau, Macau 999078, China, on leave from the Instituto Superior Técnico, Universidade de Lisboa, 1049-001 Lisbon, Portugal (e-mail: rmartins@um.edu. mo).

Color versions of one or more of the figures in this article are available online at http://ieeexplore.ieee.org.

Digital Object Identifier 10.1109/TVLSI.2019.2915769

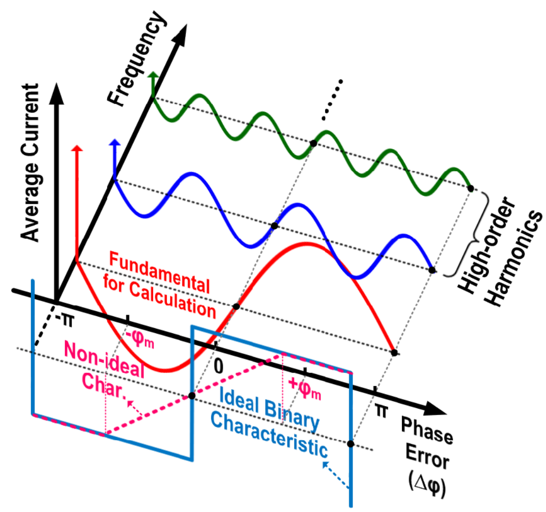

Fig. 1. Ideal transfer characteristic (solid line) of the BBPD and its Fourier series as well as a smoothing binary characteristic (dashed line).

Fig. 1 depicts the ideal characteristic of a generic BBPD where its binary operation quantizes the positive and negative phase errors between the input pattern and the output clock of the voltage-controlled oscillator (VCO), corresponding to a strongly nonlinear phase-to-voltage conversion. However, the nonlinear behavior of the BBPD-based CDR (BBCDR) loop complicates its analysis and design.

Internal and external jitters incur an undesirable bit error at the output of the BBCDR. The jitter transfer function (JTF), jitter tolerance (JTOL), and jitter generation (JGEN) mainly determine the specification of the BBCDR frequency response and they confront a tradeoff among them. For JTF, a narrow loop bandwidth (BW) is preferable to suppress high-frequency disturbance, but a small loop BW cannot effectively suppress the VCO phase noise, exacerbating the JGEN. Moreover, a large loop BW is desirable to aid the JTOL. To surmount these tradeoffs, an accurate method aiming for jitter analysis is essential for evaluating the jitter performance of the BBCDR.

Past effort has been focused on the hard nonlinearity of the BBCDR [17]–[27]. Almost none of the previous works offers a thorough analysis of a third-order BBCDR loop, i.e., the BBCDR employs just a second-order loop filter (LF). A nonlinear stochastic analysis based on the Markov model has been applied to evaluate the effect of the timing jitter [17]–[20], but only the first-order BBCDR loop was well studied. The analysis in [21] is extended to the second-order BBCDR loop for the intersymbol interference and the JTOL evaluation, but the analysis of JTF and JGEN is still missing. The phase-domain models of the first- and second-order BBCDRs in [22] are developed separately, while underlining the dynamic characteristic of the BBCDR loop. An event-driven model reported in [23] obtains fast verification. Regrettably, both [22] and [23] do not pay much attention to the jitter specification mentioned above.

There are other prior works [24]–[27] studying the foregoing characteristic of the second-order BBCDR loop. The phase-domain model in [24] is similar to [22] and is only useful for the JTOL analysis without the analysis of JTF and JGEN. Lee *et al*. [25] calculates the JTOL, JTF, and JGEN based on the dynamic time-domain waveform, but they presume a geometric approximation and a large off-chip LF that may not hold in a fully-integrated circuit. Adrang and Miar-Naimi [26] propose a method using the Fourier series, combined with the time-domain waveform to predict the jitter specification. All aforementioned works have not investigated the jitter features of the third-order BBCDR loop.

In many practical applications, the utilization of a second-order LF restrains the disturbance on the control side of the VCO. Cheng *et al*. [27] analyzes the stable oscillation mode based on the steady-state waveforms of a third-order phase-locked loop (PLL) with the BBPD, but fail to predict the jitter performance. In this paper, we detail the jitter analysis of a generic third-order BBCDR characterized by the Fourier series and time-domain waveforms. We derive the closed-form equations of both JTF and JTOL, and the simplified equation of the JGEN based on the fundamental (Fig. 1), with the nonideal phenomenon explained in detail. Finally, the behavioral simulation developed in the MATLAB/Simulink program verifies our analysis.

After this introduction, we overview the architecture of the third-order BBCDR and detail our time-domain waveform-based analytical method. Sections III and IV provide the JTF and JTOL analysis, respectively, whereas Section V focuses on the JGEN. Section VI evaluates the accuracy of our analytical methods using the behavioral simulations. Finally, Section VII draws the conclusion.

II. Architecture and Analytical Methods of Third-Order Full-Rate BBCDR

Fig. 2 shows the architecture of the typical third-order full-rate BBCDR. The function of the BBPD, namely, *Alexander phase detector* [28], is to sense the phase error between the centers of the incoming data (D_{in}) and recovered clock (CK_{out}) from the VCO, and simultaneously deliver the retimed data (D_{out}). The BBPD outputs the “Early” and “Late” signals to the succeeding charge pump (CP), indicating that the sign of the phase error between its inputs, i.e., the recovered clock is leading or lagging the input data [28]. The CP supplies the BBPD outputs to charge or discharge the second-order LF consisting of R_1, C_1, and C_2, for adjusting the VCO control voltage (V_{cont}) so as to reduce the phase error.

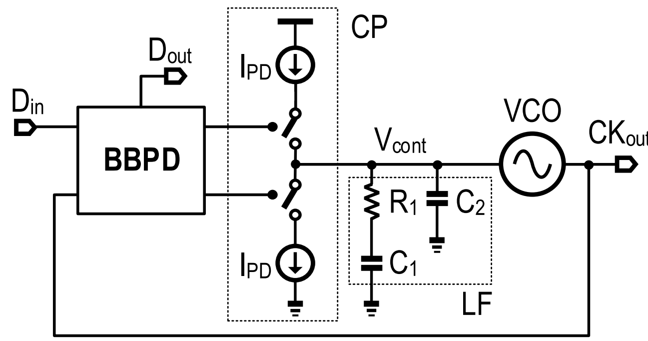

Fig. 2. Third-order full-rate BBCDR with a generic BBPD.

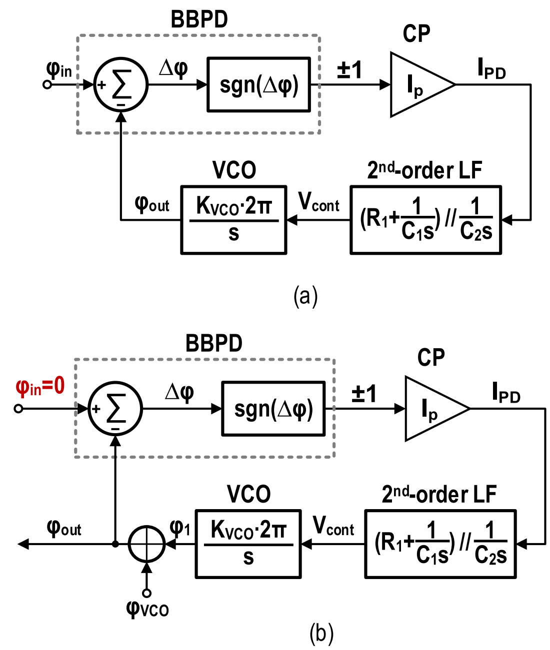

Fig. 3. Phase-domain behavior models for (a) JTF and JTOL and (b) JGEN corresponding to the diagram in Fig. 2.

In practical systems, extra C_2 is usually added in parallel with R_1 and C_1 to suppress any sudden artifacts on V_{cont}, which is produced by the charge injection and clock feedthrough of the two switches, thereby improving the transient characteristics. Generally, we have $C_2 \ll C_1$, but it increases the order of the feedback loop and induces certain nonideal phenomenon. In fact, a quantitative analysis proved to be useful for the choice of C_2, instead of selecting a capacitor based on the rule of thumb. Fig. 3 presents the behavior models of a third-order BBCDR. The BBPD is modeled as a phase subtractor followed by a sign function [sgn()]. The second-order LF is defined by its transfer function, while the VCO operates as a phase integrator. K_{VCO} is the VCO gain and I_{PD} is the time-varying current flowing through the LF. Both JTF and JTOL evaluations focus on the output jitter depending on the input jitter, while JGEN concerns about the output jitter induced by the intrinsic noise. Therefore, two separated models are implemented in MATLAB/Simulink to verify the accuracy of our analysis, according to Fig. 3(a) and (b), respectively.

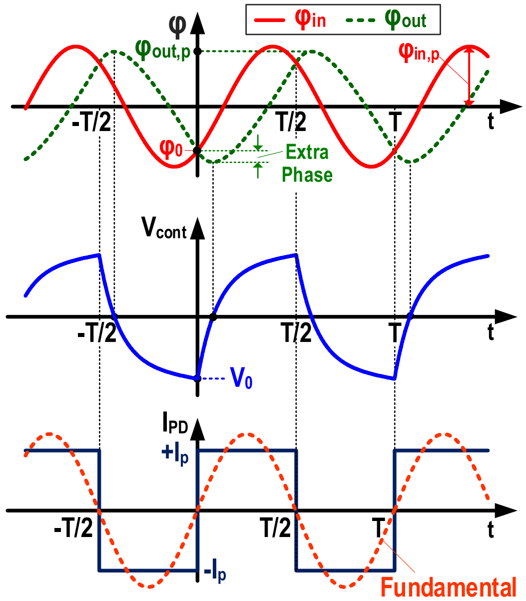

Fig. 4. Time-domain waveforms in slewing region.

Considering that a sinusoidal jitter is injected as φ_{in} in Fig. 3(a), when the BBCDR loop experiences the full slewing region, we obtain the steady-state time-domain waveforms as shown in Fig. 4. We denote f_{jitter} as input jitter frequency. It is obvious that φ_{out} tracks φ_{in} with the same period T (i.e., $T = 1/f_{\text{jitter}}$). We define $\Delta\varphi$ as the phase difference between φ_{in} and φ_{out}. Every time φ_{out} catches up with φ_{in}, the reversed-sign $\Delta\varphi$ changes the polarity of I_{PD}, thus producing a periodic square waveform. However, the charged capacitors in LF prevent V_{cont} from changing the polarity immediately. Therefore, an extra phase appears on φ_{out}, which results in the jitter peaking (JP) when $\varphi_{\text{out,p}} > \varphi_{\text{in},p}$.

The impulse response (h_1) of I_{PD} to φ_{out} in Fig. 3(a) can be deduced from the corresponding transfer function (H_1)

$$H_1(s) = \frac{R_1C_1s+1}{R_1C_1C_2s^2+(C_1+C_2)s}\cdot\frac{K_{\text{VCO}}}{s}$$
$$h_1(t) = K_{VCO}\left[\frac{t}{C_1+C_2}+\frac{R_1C_{\text{eq}}^2}{C_2^2}\left(1-e^{-\frac{1}{R_1C_{\text{eq}}}t}\right)\right]u(t) \tag{1}$$

where $C_{\text{eq}} = C_1C_2/(C_1+C_2)$. Under $0 \le t \le T/2$, by the aid of the Fourier series, the periodic function $I_{\text{PD}}(t)$ can be expanded as

$$I_{PD}(t) = \frac{4I_p}{\pi}\sum_{n=1}^{+\infty}\left[\frac{1}{n}\sin(n\omega_p t)\right] \quad n \text{ is odd} \tag{2}$$

where $\omega_p = 2\pi f_{\text{jitter}}$. By convoluting $I_{\text{PD}}(t)$ with $h_1(t)$, $\varphi_{\text{out}}(t)$ can be expressed by

$$\varphi_{\text{out}}(t) = \sum_{n=1}^{+\infty}\left\{\frac{\alpha}{n}\int_{-\infty}^{+\infty}\sin[n\omega_p(\tau-t)]\right.$$
$$\left.\times\left[\tau+\frac{R_1C_{eq}}{k}\left(1-e^{-\frac{1}{R_1C_{eq}}\tau}\right)\right]u(\tau)d\tau\right\} \tag{3}$$

where $k = C_2/C_1$ and

$$\alpha = \frac{4K_{\text{VCO}}I_p}{\pi(C_1+C_2)}. \tag{4}$$

To get the closed-form solution, we rearrange (3) as

$$\varphi_{\text{out}}(t)$$
$$= -\sum_{n=1}^{+\infty}\frac{\alpha}{n}\left\{\left(\frac{1}{n^2\omega_p^2}+\frac{R_1^2C_{eq}^2}{k\left(1+n^2\omega_p^2R_1^2C_{eq}^2\right)}\right)\sin(n\omega_p t)\right.$$
$$+\left(\frac{R_1C_{eq}}{kn\omega_p}-\frac{n\omega_pR_1^3C_{eq}^3}{k\left(1+n^2\omega_p^2R_1^2C_{eq}^2\right)}\right)\cos(n\omega_p t)$$
$$+\left[\left(\frac{\tau-t}{n\omega_p}-\frac{R_1C_{eq}}{kn\omega_p}\right)\cos(n\omega_p\tau)\right.$$
$$\left.\left.\left.-\frac{1}{n^2\omega_p^2}\sin(n\omega_p\tau)\right]\right|_{\tau=-\infty}\right\}. \tag{5}$$

Fig. 4 (top) shows $\varphi_{\text{out}}(0) = \varphi_{\text{out}}(T)$, and we can obtain $\cos(n\omega_p\tau)|_{\tau=-\infty} = 0$. Similarly, due to $-\varphi_{\text{out}}(0) = \varphi_{\text{out}}(T/2)$, we will have $\sin(n\omega_p\tau)|_{\tau=-\infty} = 0$ when n is odd. Thus, (5) can be further simplified as

$$\varphi_{\text{out}}(t) = -\sum_{n=1}^{+\infty}\left\{\frac{\alpha}{n}[(A_n+B_n)\sin(n\omega_p t)\right.$$
$$\left.+n\beta(C_1A_n-C_2B_n)\cos(n\omega_p t)]\right\} \tag{6}$$

where

$$\beta = \frac{\omega_pR_1C_{\text{eq}}}{C_2}. \tag{7}$$

The Fourier coefficients A_n and B_n are determined by

$$A_n = \frac{1}{n^2\omega_p^2} \tag{8}$$

$$B_n = \frac{R_1^2C_{\text{eq}}^2}{k\left(1+n^2\omega_p^2R_1^2C_{\text{eq}}^2\right)}. \tag{9}$$

Note that $\varphi_{\text{out}}(t)$ in (6) is an infinite sum of the orthogonal sines and cosines involving a series of high-order harmonics. Due to the low-pass properties of $H_1(s)$, the loop characteristic is dominated by the fundamental. Considering that the high-order harmonics contribute slightly to φ_{out}, that is,

$$|\varphi_{\text{out}}(\omega_p t)| \gg |\varphi_{\text{out}}(n\omega_p t)|, \quad n = 3, 5, \ldots \tag{10}$$

We simplify (6)–(11) with the fundamental, which will be used in the following analysis:

$$\varphi_{\text{out}}(t) = -\alpha[(A_1+B_1)\sin(\omega_p t)$$
$$+\beta(A_1C_1-B_1C_2)\cos(\omega_p t)] \tag{11}$$

where

$$A_1 = \frac{1}{\omega_p^2} \tag{12}$$

$$B_1 = \frac{R_1^2C_{\text{eq}}^2}{k(1+\omega_p^2R_1^2C_{\text{eq}}^2)} \tag{13}$$

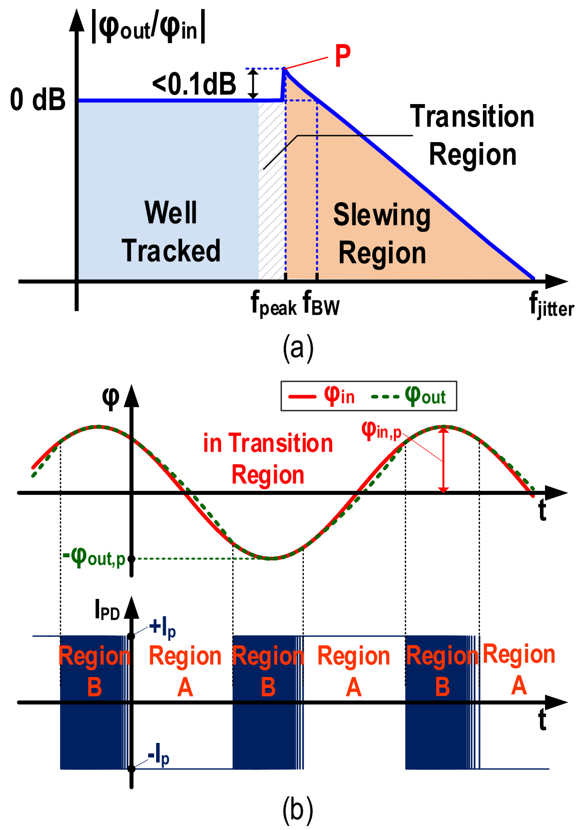

Fig. 5. (a) JTF with JP. (b) Illustration of the time-domain waveforms in the transition region obtained from the MATLAB/Simulink model with loop parameters in Table I.

Setting $t = 0$ in (11), the initial phase φ_0 of $\varphi_{\text{out}}(t)$ is written as

$$\varphi_0 = \alpha\beta(B_1C_2 - A_1C_1) \tag{14}$$

The above equations are developed for describing the time-domain waveforms in the slewing region and obtaining basic mathematical expressions for $\varphi_{\text{out}}(t)$ and its initial phase φ_0. They will be used in Sections III and IV for further analysis. In particular, (15) and (25) directly use them, and we will obtain JTOL_1 in (28), JTOL_2 in (29), and JTOL_3 in (32).

III. Jitter Transfer Analysis

The JTF of the BBCDR is defined as the ratio of output jitter to the input jitter across f_{jitter}. Fig. 5(a) shows that the JTF of the BBCDR exhibits a low-pass characteristic with a sharp rise coming from the ideal bang-bang characteristic of BBPD. If the input jitter varies slowly, the output tracks the input closely to ensure phase locking, resulting in $|\varphi_{\text{out}}/\varphi_{\text{in}}| \approx 1$ (0 dB). However, when the BBCDR loop enters the slewing region, φ_{out} can hardly track φ_{in}, thus reducing $|\varphi_{\text{out}}/\varphi_{\text{in}}|$. The JP happens near the lower bound of the slewing region at point "P" in Fig. 5(a), and the corresponding f_{jitter} is defined as f_{peak}. Extrapolation of well-tracked and slewing regions yields the approximated BW (f_{BW}) of JTF [25]. Practically, JTF must meet the requirements specification. For example, the JTF peaking should be <0.1 dB. Interestingly, f_{BW} approaches f_{peak} as JP decreases.

Fig. 5(b) shows the time-domain waveforms in the transition region, where f_{jitter} is slightly smaller than f_{peak}. Different from the periodic I_{PD} (Fig.4, lower), I_{PD} in this region is no longer a periodic square waveform. It can be divided into two dynamic parts: Region A and Region B. In Region A, the well-tracked condition disables, leading to long-run $+I_p$ or $-I_p$. Inversely, in Region B, I_{PD} varies rapidly and φ_{out} tracks φ_{in} in the vicinity of $\varphi_{\text{in},p}$. Although φ_{in} is large in Region B and small in Region A, the slope of φ_{in} is smaller in Region B than that in Region A. When φ_{out} tracks φ_{in}, they share the same magnitude and slope. Note that the tracking ability of a BBCDR is determined by the maximum slope of φ_{out} rather than the absolute magnitude of φ_{out}. It is worth of mentioning that $\varphi_{\text{out}} \approx \varphi_{\text{in}}$ leads to a 0-dB JTF, indicating that JP happens in the slewing region. As f_{jitter} decreases, Region B expands, and the BBCDR loop enters the well-tracked region gradually. Inversely, its operation in the Region A will be extended. If Region B fades, I_{PD} in Fig. 5(b) will return to that in Fig. 4.

A. Derivation of f_{BW}

Based on (11), $\varphi_{\text{out,p}}$ is easy to be deduced as

$$\varphi_{\text{out},p}(f) = \alpha\sqrt{(A_1 + B_1)^2 + [\beta(A_1C_1 - B_1C_2)]^2} \tag{15}$$

When f_{jitter} is close to f_{BW}, we can assume $|\varphi_{\text{out,p}}/\varphi_{\text{in,p}}| \approx 1$, and then we obtain the following equations:

$$(A_1 + B_1)^2 + \beta^2(A_1C_1 - B_1C_2)^2 = \frac{\varphi_{\text{in},p}^2}{\alpha^2} \tag{16a}$$

$$\left(\frac{\varphi_{in,p}^2\omega_p^4}{\alpha^2} - \frac{\omega_p^2 R_1^2 C_1^2}{1+k}\right)\left(1 + \omega_p^2 R_1^2 C_2^2\right) - 1 = 0 \tag{16b}$$

A further approximation with the consideration of $2R_1C_2f_{\text{BW}} \ll 1$ results in

$$f_{\text{BW}} = \sqrt{\frac{\alpha^2 R_1^2 C_1^2 + (1+k)\alpha^2\sqrt{\sigma}}{8\pi^2(1+k)\varphi_{\text{in},p}^2}} \propto \sqrt{\frac{1}{(1+k)^3}} \tag{17}$$

where

$$\sigma = \frac{R_1^4 C_1^4}{(1+k)^2} + \frac{4\varphi_{\text{in},p}^2}{\alpha^2} \tag{18}$$

Because f_{BW} is proportional to $1/\sqrt{(1+k)^3}$, i.e., C_2 appears only in the denominator, we observe that f_{BW} decreases along with the increment of C_2.

B. Slope of JTF in the Slewing Region

Based on (15), JTF in the slewing region can be written as

$$\frac{\varphi_{\text{out},p}}{\varphi_{\text{in},p}}(f) \approx \rho\sqrt{(A_1 + B_1)^2 + [\beta(A_1C_1 - B_1C_2)]^2} \tag{19}$$

where $\rho = \alpha/\varphi_{\text{in},p}$. Interestingly, the simulation results depart from the ideal second-order slope (−40 dB/dec). According to (12) and (13), ρA_1 and ρB_1 are both second-order terms, while the second-order pole of ρB_1 may occur after f_{BW}.

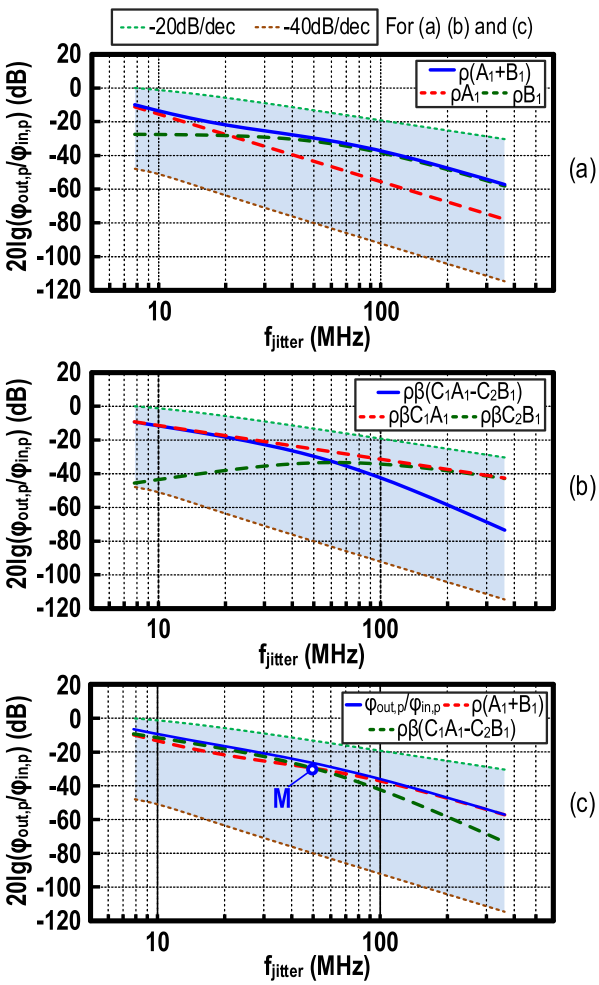

Fig. 6. Slope comparison for the different terms in (19).

Thus, $\rho(A_1+B_1)$ turns out to fall with a slope of -40 dB/dec, and is almost in full frequency range with a flat area, as shown in Fig. 6(a). For the second term, $\rho\beta A_1 C_1$ is first-order while $\rho\beta C_2 B_1$ has a zero at the origin and a complex-conjugate pole pair. Both terms decrease at a slope of -20 dB/dec at the frequency of interest, and their difference $(\rho\beta C_1 A_1 - \rho\beta C_2 B_1)$ shows a high-order slope [Fig. 6(b)]. The total slope of $\varphi_{\text{out,p}}/\varphi_{\text{in},p}$ is more close to that of $\rho(A_1+B_1)$ after the point M, since $\rho(A_1+B_1)$ is much larger than $(\rho\beta C_1 A_1 - \rho\beta C_2 B_1)$, as depicted in Fig. 6(c). It means that $\rho(A_1+B_1)\ \sin(\omega_p t)$ dominates the $\varphi_{\text{out},p}/\varphi_{\text{in},p}$ and $(\rho\beta C_1 A_1 - \rho\beta C_2 B_1)\cos(\omega_p t)$ can be neglected. It falls at the rate of -40 dB/dec in the high-frequency region. Yet, $\varphi_{\text{out},p}/\varphi_{\text{in},p}$ is -20 dB/dec rolloff in terms of f_{jitter}, when $(\rho\beta C_1 A_1 - \rho\beta C_2 B_1)$ dominates $\varphi_{\text{out},p}/\varphi_{\text{in},p}$ before the point M. Therefore, the slope near the point M, which locates behind f_{BW}, may even be -20 dB/dec.

C. Jitter Peaking

Referring to the above analysis, JP happens when φ_{out} catches up with φ_{in} at the minimum of input phase, i.e., $-\varphi_0 = \varphi_{\text{in},p}$. It will be observed later in Fig. 11(c) in Section VI-B.

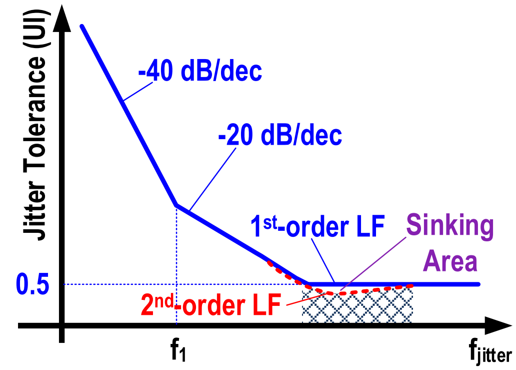

Fig. 7. Typical JTOL of the BBCDR with a first-order LF (solid line) and a second-order LF (dashed line).

We rearrange the above equation in regard to f_{peak} as follows:

$$\varphi_{\text{in},p} + \varphi_0(f_{\text{peak}}) = 0. \tag{20}$$

Thus, f_{peak} can be solved from (14) and (20), and JP can be solved by substituting f_{peak} into (19)

$$JP \approx \rho\sqrt{(A_1+B_1)^2 + \left[2\pi R_1 C_{\text{eq}} f_{\text{peak}}\left(\frac{A_1}{k} - B_1\right)\right]^2} \tag{21}$$

IV. Jitter Tolerance Analysis

The JTOL is a widely used specification to estimate the ability of retiming a jittered input pattern. It specifies the maximum $\varphi_{\text{in},p}$ that can be tolerated by the system without increasing the bit error rate (BER). An approximate condition to avoid increasing the BER is $|\varphi_{\text{in}} - \varphi_{\text{out}}| < 0.5$ UI. Fig. 7 illustrates the typical JTOL curves with first- and second-order LFs. JTOL falls at the slope of -40 dB/dec prior to f_1, and turns to -20 dB/dec afterward, they approach 0.5 UI finally. For the BBCDR with a second-order LF, there is a sinking area, which is different from that of a first-order LF. Detailed time-domain explanation will be discussed in Section VI-C.

It is noteworthy that the BBCDR must experience the full slewing if bit error occurs, otherwise, φ_{out} tracks φ_{in} well, and the data can be sampled correctly. Normally, a sinusoidal jitter is applied to evaluate the JTOL. As illustrated in Fig. 8, φ_{in} can be expressed as follows:

$$\varphi_{\text{in}}(t) = -\varphi_{\text{in},p}\sin(\omega_p t - \theta_0) \tag{22}$$

where θ_0 is the initial phase of the input jitter. Combining (22) with (14), we can write

$$\varphi_{\text{in},p}\sin\theta_0 = \varphi_0 = \alpha\beta(B_1 C_2 - A_1 C_1). \tag{23}$$

Due to $\cos\theta_0 = \sin(\pi/2 + \theta_0)$, $\cos\theta_0$ must be negative (Fig. 8). Thus, we obtain

$$\varphi_{\text{in},p}\cos\theta_0 = -\sqrt{\varphi_{\text{in},p}^2 - \varphi_0^2}. \tag{24}$$

$\Delta\varphi(t)$ is obtained by substituting (22) and (11) into $\varphi_{\text{in}}(t)$ and $\varphi_{\text{out}}(t)$

$$\begin{aligned}\Delta\varphi(t) &= \varphi_{\text{in}}(t) - \varphi_{\text{out}}(t)\\ &= [\varphi_0 + \alpha\beta(A_1 C_1 - B_1 C_2)]\cos(\omega_p t)\\ &\quad + \left[\sqrt{\varphi_{\text{in},p}^2 - \varphi_0^2} + \alpha(A_1+B_1)\right]\sin(\omega_p t).\end{aligned} \tag{25}$$

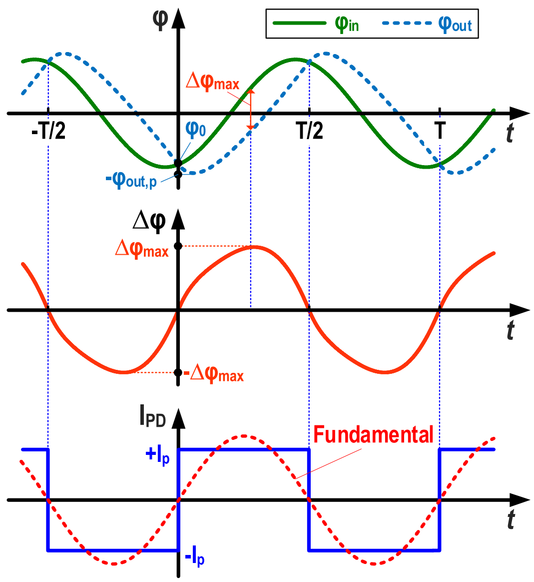

Fig. 8. Time-domain waveforms in the slewing region for JTOL evaluation.

Substituting (23) and (24) into (25), $\Delta\varphi$ is rewritten as

$$\Delta\varphi(t) = \left[\sqrt{\varphi_{\mathrm{in},p}^2 - \varphi_0^2} + \alpha(A_1 + B_1)\right]\sin(\omega_p t). \tag{26}$$

Hence, $\Delta\varphi_{\max}$ is calculated as

$$\Delta\varphi_{\max} = \sqrt{\varphi_{\mathrm{in},p}^2 - \varphi_0^2} + \alpha(A_1 + B_1). \tag{27}$$

Equating $\Delta\varphi_{\max}$ to 0.5 UI yields the JTOL at f_{jitter}

$$\mathrm{JTOL}_1 = \sqrt{\left[\frac{1}{2} - \alpha(A_1 + B_1)\right]^2 + \varphi_0^2}. \tag{28}$$

For simplicity, 0.5 UI can be expressed as 1/2 rather than π, if the unit of K_{VCO} is Hz/V. Also, when C_2 is ignored compared to C_1, JTOL_2 is obtained as

$$\mathrm{JTOL}_2 \approx \sqrt{\left[\frac{1}{2} - \frac{4K_{\mathrm{VCO}}I_p}{\pi C_1}(a_1 + b_1)\right]^2 + \varphi_0^2} \tag{29}$$

where

$$a_1 = \frac{1}{\omega_p^2} \tag{30}$$

$$b_1 = \frac{R_1^2 C_1 C_2}{1 + \omega_p^2 R_1^2 C_2^2}. \tag{31}$$

The effect of C_2 on JTOL is nonlinear. In the low-frequency region, JTOL decreases as C_2 increases. Inversely, JTOL rises depending on C_2 in the high-frequency region. To verify the above derivation, φ_0 in (25) is replaced by the second-order counterpart [26], i.e., $\pi K_{\mathrm{VCO}} I_p R_1 / 2\omega_P$. With the assumption of $f \ll (2\pi R_1\sqrt{C_1 C_2})^{-1}$, JTOL_3 can be deduced from (28)

$$\mathrm{JTOL}_3 = \left\{\left[\sqrt{\frac{1}{4} - \left(\frac{K_{\mathrm{VCO}} I_P R_1}{\omega_P}\frac{8-\pi^2}{2\pi}\right)^2} - \frac{4K_{\mathrm{VCO}} I_P}{\pi C_1}\frac{1}{\omega_P^2}\right]^2 + \left(\frac{\pi}{2}\frac{K_{\mathrm{VCO}} I_P R_1}{\omega_P}\right)^2\right\}^{\frac{1}{2}} \tag{32}$$

which is the same as the result in [26].

V. Jitter Generation Analysis

The JGEN describes the jitter arising from various sources such as VCO phase noise, crosstalk, and supply voltage disturbance. It appears as the output jitter when there is no jitter injected from outside. Here, we study the contribution of VCO phase noise to the output of the BBCDR. For JGEN verification, a model can be established by adding an extra sinusoidal jitter to VCO phase noise, without jitter at the input [Fig. 3(b)].

The loop gain (LG) of the third-order BBCDR is demonstrated as

$$\mathrm{LG}(s) = \frac{K_{\mathrm{PD}} I_P K_{\mathrm{VCO}}(R_1 C_1 s + 1)}{(R_1 C_1 C_2 s + C_1 + C_2)s^2} \tag{33}$$

where K_{PD} is the gain of the BBPD. It has three poles and one zero, with two poles at the origin and the zero below the last pole. JGEN in (34) and JTF in (35) are deduced. In addition, we can obtain JTOL in (36) by equating $\Delta\varphi$ to 0.5 UI

$$\mathrm{JGEN}(s) = \frac{1}{1 + \mathrm{LG}(s)} \tag{34}$$

$$\mathrm{JTF}(s) = \frac{\mathrm{LG}(s)}{1 + \mathrm{LG}(s)} \tag{35}$$

$$\mathrm{JTOL}(s) = \frac{1}{2}[1 + \mathrm{LG}(s)]. \tag{36}$$

It is obvious that the denominator in (34) is negative, when $s < -1/R_1 C_{\mathrm{eq}}$. If $s > -1/R_1 C_1$, this denominator is positive. Real poles of JGEN only appear within $(-1/R_1 C_{\mathrm{eq}}, -1/R_1 C_1)$. In general, complex poles are also located in above interval. Yet, there are two zeros at the origin and the last zero appears when $s = -1/R_1 C_{\mathrm{eq}}$. It implies that JGEN has a high-pass profile. Because of the denominator of JTF and the numerator of JTOL are the same as the denominator of JGEN, they have the same corner frequency.

Similar to the JTOL analysis, φ_{VCO} and φ_{out} can be viewed as φ_{in} and $\Delta\varphi$ in Fig. 3(a), respectively. Thus, the following equation can be written directly according to (27):

$$\varphi_{\mathrm{out},p} = \sqrt{\varphi_{\mathrm{VCO},p}^2 - \varphi_0^2} + \alpha(A_1 + B_1). \tag{37}$$

Thus, JGEN can be expressed as

$$\mathrm{JGEN} = \frac{\sqrt{\varphi_{\mathrm{VCO},p}^2 - \varphi_0^2} + \alpha(A_1 + B_1)}{\varphi_{\mathrm{VCO},p}}. \tag{38}$$

This result holds when the BBCDR enters the full slewing region as shown in Fig. 5. Consider $2\pi R_1 C_2 f \gg 1$ and $C_2 \ll C_1$, we can simplify (38) as

$$\mathrm{JGEN} = 1 + \frac{4K_{\mathrm{VCO}} I_p}{\pi \varphi_{\mathrm{VCO},p} C_2 \omega_p^2}. \tag{39}$$

JGEN decreases as C_2 increases. We can observe that: 1) when ω_p rises, JGEN approaches 0 dB and 2) since the second term in (39) is positive, JGEN is larger than 0 dB, indicating that the peaking always exists in the third-order BBCDR loop.

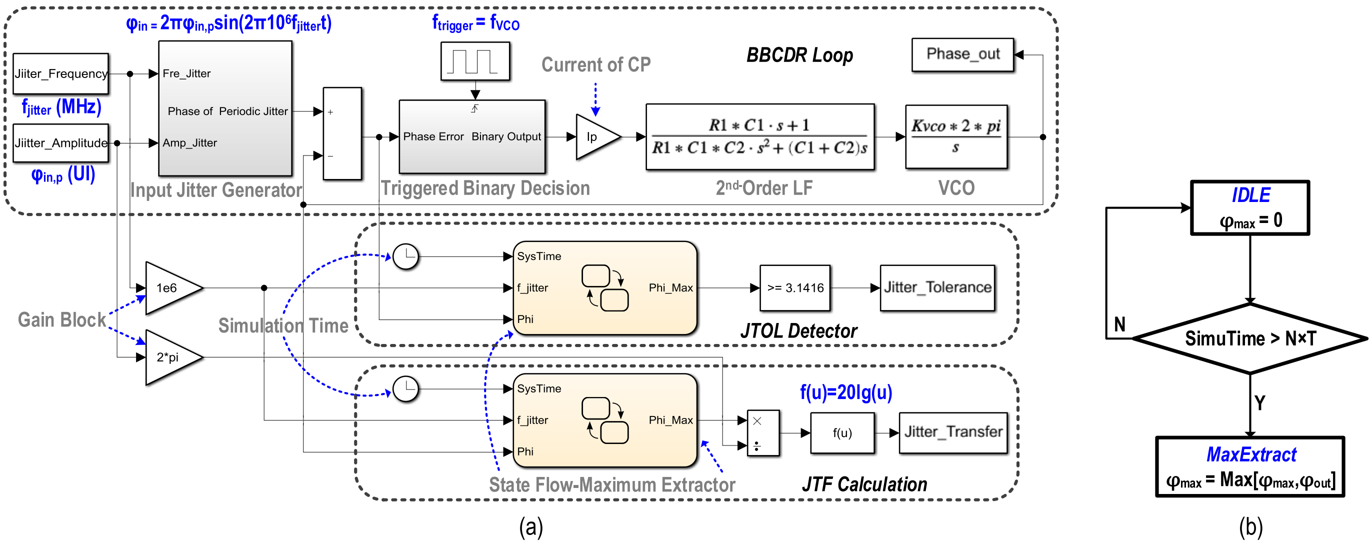

Fig. 9. (a) MATLAB/Simulink model for JTF and JTOL verification. (b) Algorithm of the state flow *Maximum Extractor*.

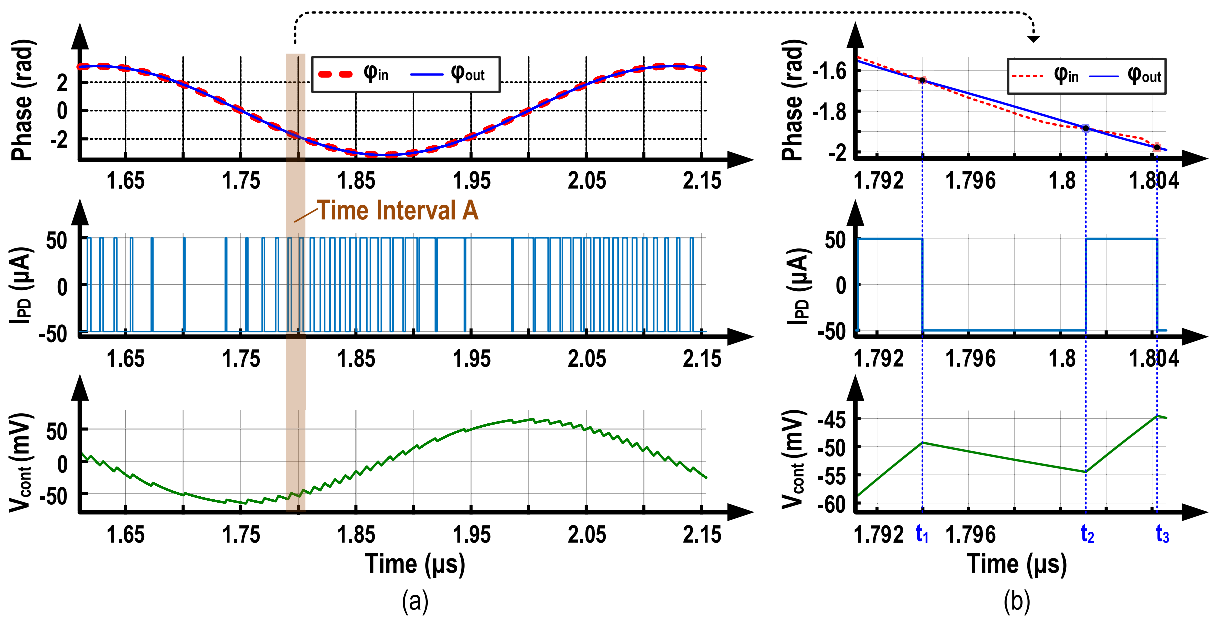

Fig. 10. Time-domain waveforms corresponding to the well-tracked region in Fig. 5. The loop parameters of LP-I in Table I are preset with $\varphi_{\text{in},p} = 0.5$ UI and $f_{\text{jiiter}} = 2$ MHz. (a) Steady-state waveforms of φ_{in}, φ_{out}, V_{cont}, and I_{PD}. (b) Zoomed-in detail in the time interval A in (a), where t_1, t_2, and t_3 are the three time instants corresponding to the intersection of φ_{in} and φ_{out}.

VI. Behavioral Simulations and Discussions

A. MATLAB/Simulink Model

To validate the results derived in the previous section, we develop the top-level behavior model in MATLAB/Simulink for JTF and JTOL verification, as shown in Fig. 9(a). It mainly consists of three parts: 1) the BBCDR loop corresponding to the phase-domain model [Fig. 3(a)]; 2) the *JTOL Detector* block; and 3) the *JTF Calculation* block. In the BBCDR loop, the subsystem *Input Jitter Generator* provides a sinusoidal jitter, which is expressed by $\varphi_{\text{in}} = 2\pi\varphi_{\text{in},p}\sin(2\pi\, 10^6 f_{\text{jitter}} t)$. The subsystem *Triggered Binary Decision* operates with the beat of a pulse signal periodically, whose frequency is equal to f_{VCO}, i.e., the frequency of the VCO. Fig. 9(b) shows the algorithm of *Maximum Extractor*. In the *IDLE* state, $\varphi_{\max}$ is assigned to zero, and the simulation time of the system will be compared to a threshold time in terms of f_{jitter}. If the simulation time is larger than $N \cdot T$, which indicates the third-order BBCDR loop operating steadily, and then *MaxExtract* state returns *Max*[$\varphi_{\max}$, φ_{out}]. Otherwise, it jumps back to the *IDLE* state. Here, *Max*[] is the function to return the maximum element of inputs. We begin the simulation with an ideal binary decision and consider the nonideal effect later.

By properly setting the simulation parameters, i.e., *Stop time* of the simulation and *Max step size* of the solver, we can obtain a good tradeoff between the simulation accuracy and efficiency. The *Stop time* of simulation is set according to

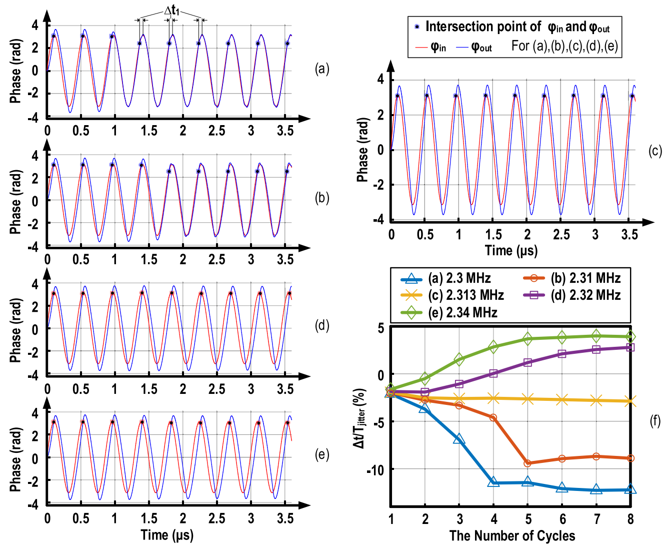

Fig. 11. Time-domain waveforms around f_{peak} and their tendency. The loop parameters of LP-I in Table I are preset for simulation with $\varphi_{\text{in},p} = 0.5$ UI. (a) $f_{\text{jitter}} = 2.3$ MHz. (b) $f_{\text{jitter}} = 2.31$ MHz. (c) $f_{\text{jitter}} = 2.313$ MHz. (d) $f_{\text{jitter}} = 2.32$ MHz. (e) $f_{\text{jitter}} = 2.34$ MHz. (f) Normalized time difference between the peaking of φ_{in} and the intersection point, corresponding to case (a)–(e), respectively.

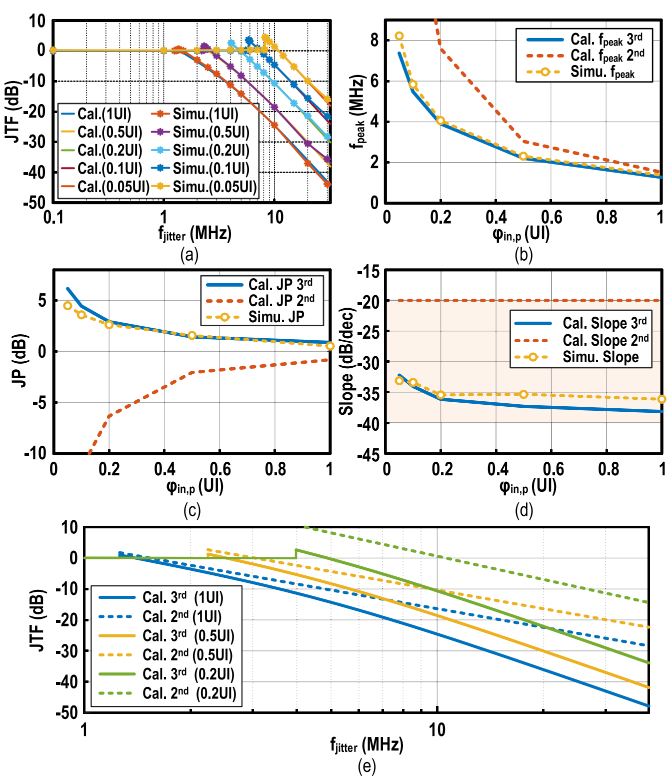

Fig. 12. Simulation and calculation results JTF with the loop parameters of LP-I in Table I. The input jitter amplitude, $\varphi_{\text{in},p}$ varies from 0.05 to 1 UI. (a) JTF under different $\varphi_{\text{in},p}$ from (19). (b) f_{peak} of JTF from (20). (c) JP from (21). (d) Slope in slewing region versus $\varphi_{\text{in},p}$. (e) JTF comparison between second-and third-order calculation results, where the second calculation results use the same equations but preset C_2 to 0.

f_{jiiter}, for example, *Stoptime* $= 10/f_{\text{jitter}}$ when $f_{\text{jitter}} < 1$ MHz and *Stoptime* $= 100/f_{\text{jitter}}$ when $f_{\text{jitter}} > 30$ MHz, and *Max step size* is preset to $0.05/f_{\text{VCO}}$.

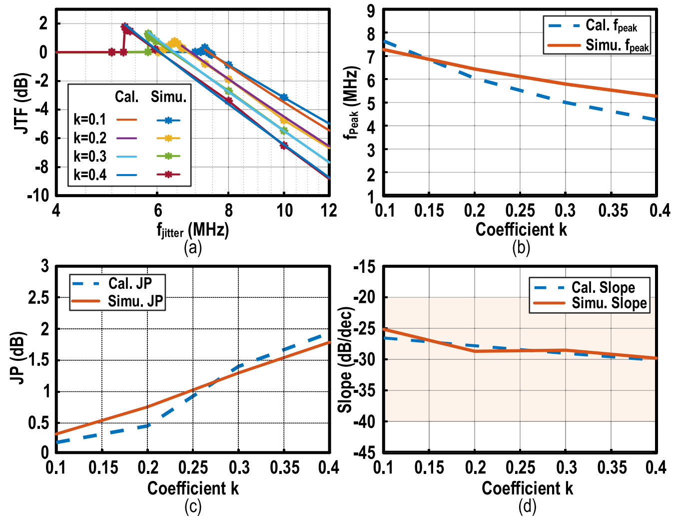

Fig. 13. Simulation and calculation results in (19) of JTF with the loop parameters of LP-II in Table I. The ratio of C_2/C_1, defined as a coefficient k, ranges from 0.1 to 0.4. (a) JTF under different k. (b) f_{peak} of JTF from (20). (c) JP from (21). (d) Slope in slewing region versus k.

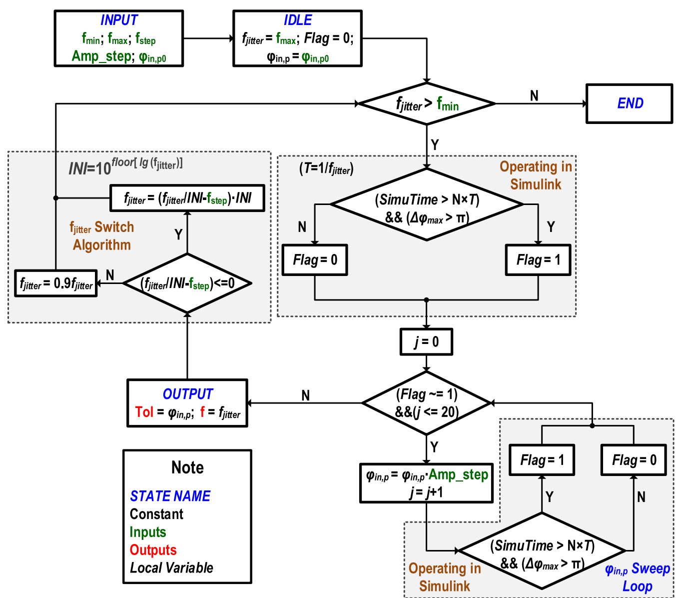

Fig. 14. Flowchart of automatic algorithm for JTOL verification.

Two sets of the loop parameters (LP) in Table I with considerable difference are used for verifying our above analysis, proving that our proposed method is not a special case only applicable to a certain loop parameter.

B. JTF Simulation

Fig. 10 shows simulated time-domain waveforms in regard to the well-tracked region in Fig. 5. The loop parameters of LP-I in Table I are preset, with $\varphi_{\text{in},p} = 0.5$ UI and $f_{\text{jiiter}} = 2$ MHz. Note that the corresponding f_{peak} is ~2.313 MHz. As shown in Fig. 10(a), φ_{out} tracks φ_{in} well and they lead each other alternatively. Thereafter, I_{PD} reverses its polarity rapidly and produces a sawtoothlike V_{cont}. Obviously, $\varphi_{\text{out}} \approx \varphi_{\text{in}}$ and a 0-dB JTF are obtained. To illustrate the details, a zoomed-in

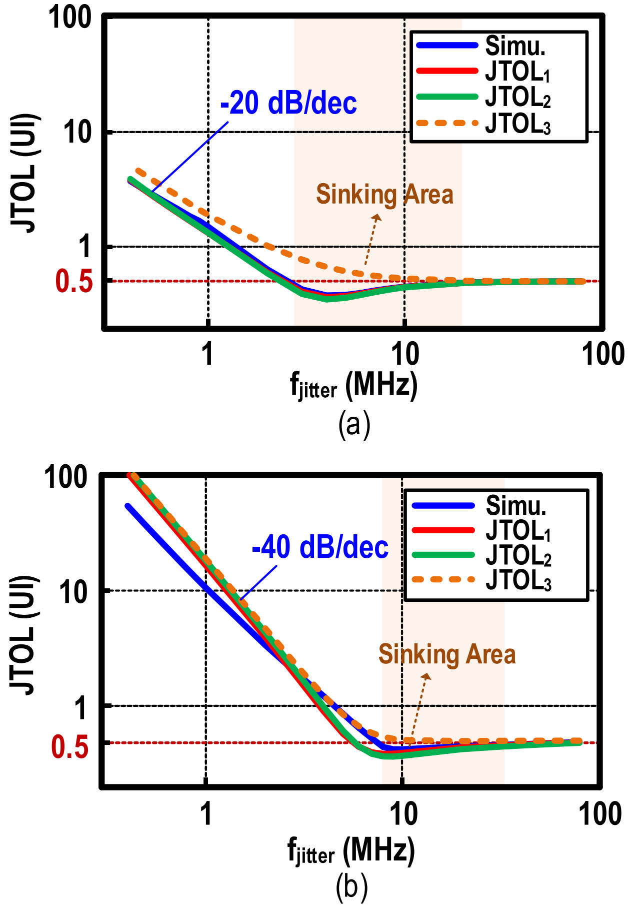

Fig. 15. Simulation and calculation results for JTOL, where $JTOL_1$, $JTOL_2$, and $JTOL_3$ are the calculation results from (28), (29), and (32), respectively. JTOL curves (a) are obtained using the loop parameters of LP-I in Table I, while JTOL curves (b) are obtained using the loop parameters of LP-II in Table I with $k = 0.1$.

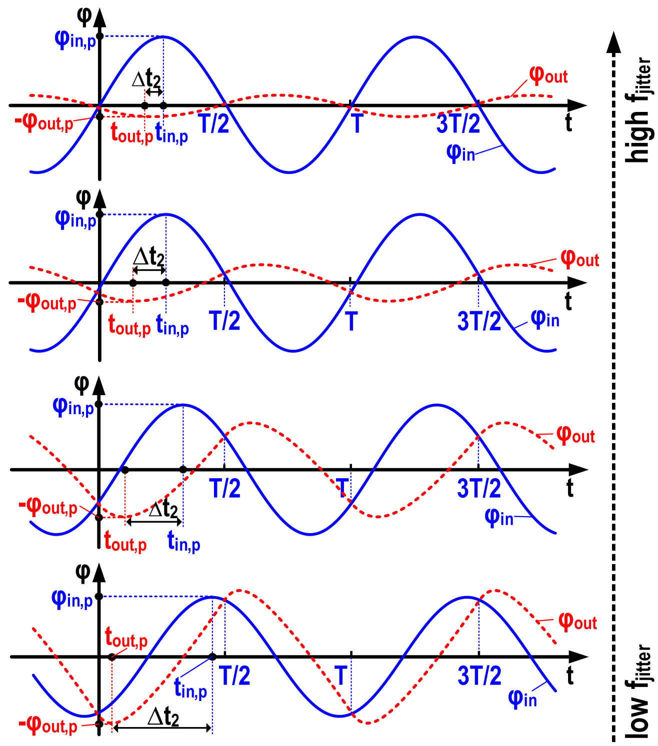

Fig. 16. Time-domain waveforms for illustrating the sinking area in the JTOL curve.

TABLE I
PARAMETERS FOR JITTER VERIFICATION

Loop Parameter Designation	LP-I	LP-II
$\varphi_{in,p}$ (UI)	variable	0.5
I_p (μA)	50	50
R_1 (Ω)	1500	400
C_1 (pF)	500	70
C_2 (pF)	25	$k{\cdot}C_1$
Coefficient k	0.05	variable
K_{VCO} (GHz/V)	0.1	0.8
Data Rate (Gb/s)	9.95328	40

view of the *Time Interval A* is shown in Fig. 10(b), where t_1, t_2, and t_3 are the time instants corresponding to the intersections of φ_{in} and φ_{out}. Between t_1 and t_2, φ_{out} exceeds φ_{in}, so that the CP generates a -50-μA I_{PD}, and V_{cont} keeps decreasing. Inversely, φ_{in} leads φ_{out}, thus the 50-μA I_{PD} pulls V_{cont} up within $[t_2, t_3]$. Fig. 11 depicts the time-domain waveforms around f_{peak}, the loop parameters preset for the simulation are also listed in Table I, namely, LP-I with $\varphi_{\text{in},p} = 0.5$ UI.

Fig. 11(a)–(e) shows the waveforms of φ_{in} and φ_{out} with the same initial condition. Δt_1 is defined as $T_{\text{IPn}} - T_n$, where T_{IPn} is the time instant of the intersection point of φ_{in} and φ_{out} in the same cycle and T_n is the nth time instant corresponding to the $\varphi_{\text{in}} = \varphi_{\text{in},p}$. When $f_{\text{jitter}} < f_{\text{peak}}$, Δt_1 keeps decreasing with the simulation time and tends to a negative constant at steady state [Fig. 11(a) and (b)]. However, when $f_{\text{jitter}} > f_{\text{peak}}$, Δt_1 shows a reverse tendency and tends to a positive steady constant [Fig. 11(d) and (e)]. When $f_{\text{jitter}} \approx f_{\text{peak}}$, Δt_1 stays almost constant during the simulation time. Fig. 11(f) shows the normalized Δt_1 versus the number of cycles, it is clear that the tendency of Δt_1 represents the location of f_{jitter} in relation with f_{peak}.

In order to validate our JTF analysis in Section III, two groups of the loop parameters of the BBCDR are simulated in the MATLAB/Simulink model, as depicted in Fig. 9. The corresponding loop parameters are used for the equations derived in Section III. In reality, φ_{in} consists of various frequency components with different $\varphi_{\text{in},p}$. However, f_{BW} is sensitive to $\varphi_{\text{in},p}$, so that the relationship between $\varphi_{\text{in},p}$ and f_{BW} must be studied. As another important parameter, C_2 suppresses the jitter due to the ripple on V_{cont} and plays a key role in the loop stability. Hence, k is also swept to provide an intuitive insight. Fig. 12 shows the simulation and calculation results of JTF with the loop parameters of LP-I in Table I. In Section III, the JTF feature depends on $\varphi_{\text{in},p}$ heavily, Fig. 12(a) depicts a cluster of JTF curves corresponding to $\varphi_{\text{in},p}$ ranging from 0.05 to 1 UI. We can observe that f_{peak} [Fig. 12(b)] decreases from 8.22 to 1.38 MHz as $\varphi_{\text{in},p}$ increases. Fig. 12(c) illustrates the monotonically decreasing function of JP, which is

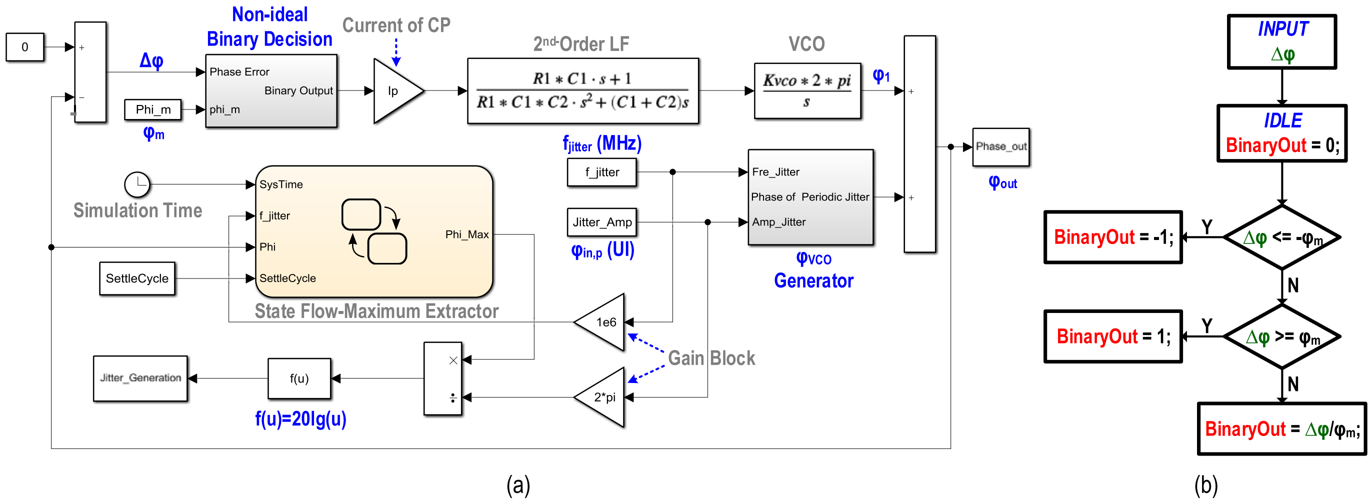

Fig. 17. (a) MATLAB/Simulink model for JGEN verification due to the VCO's phase noise, according to the phase-domain model in Fig. 3(b). (b) Algorithm for *Nonideal Binary Decision*.

reasonable considering JTF $= 20\lg\,(\varphi_{\text{out,p}}/\varphi_{\text{in},p})$. It means that a larger $\varphi_{\text{in},p}$ indicates smaller peaking. The slope in the slewing region is between -20 and -40 dB/dec and is rather flat, as shown in Fig. 12(d). Compared to the third-order calculation results from (19)–(21), the second-order calculation results are based on $C_2 = 0$, and it shows a considerable deviation from the simulation results, especially when $\varphi_{\text{in},p}$ is small. Also, the slopes from second-order calculation results are always -20 dB/dec.

Fig. 13 plots the simulation and calculation results of JTF with the loop parameters of LP-II in Table I. Note that f_{peak} decreases from 7.27 to 5.27 MHz, when k varies from 0.1 to 0.4 [Fig. 13(b)]. Although the ripple on V_{cont} is suppressed by C_2 in LF, a larger C_2 enlarges JP. When k reaches 0.4, JTF shows an undesired JP of larger than 1.5 dB [Fig. 13(c)]. Fig. 13(d) shows that the slope in the slewing region decreases slightly as k increases. The consistency between simulation and calculation results in Figs. 12 and 13 verifies our JTF analysis. To achieve a JP of <0.1 dB, k should be further smaller, and larger $\varphi_{\text{in},p}$ should be chosen comparing with those in Table I.

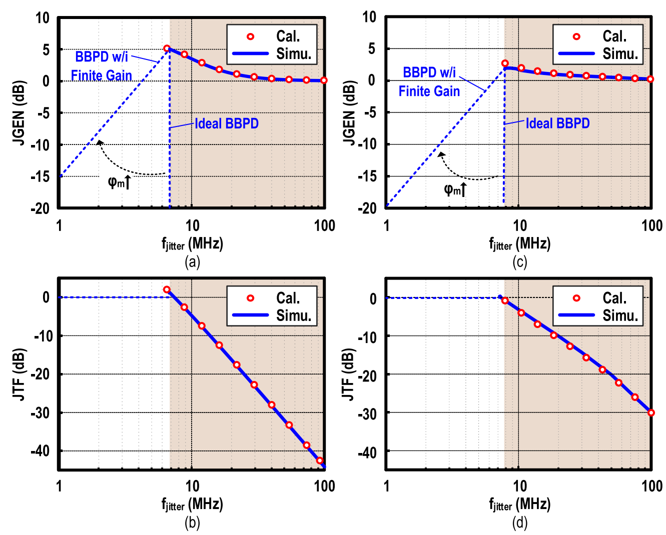

Fig. 18. Simulation and calculation results. (a) JGEN and (b) JTF using the loop parameters of LP-I in Table I with 0.1-UI $\varphi_{\text{in},p}$ ($\varphi_{\text{VCO},p}$), while (c) JGENs and (d) JTFs in are achieved using the loop parameters of LP-II in Table I with $k = 0.1$.

C. JTOL Simulation

In JTOL simulation, it is hard to determine the exact $\varphi_{\text{in},p}$ at a given f_{jitter} when the bit error occurs. Thus, we design an automatic algorithm for the JTOL verification, as shown in Fig. 14. $f_{\min}$ and $f_{\max}$ denote the lower and upper limits for the frequency of interest, respectively. The simulation starts with $f_{\text{jitter}} = f_{\max}$. f_{jitter} is compared with $f_{\min}$ at first to decide whether the simulation stops or not. If $f_{\text{jitter}} > f_{\min}$, the model activates for seeking an appropriate $\varphi_{\text{in,p}}$. Under the initial state, $\varphi_{\text{in},p}$ is set to $\varphi_{\text{in,p0}}$, and a settling time of $N \cdot T$ is entailed for steady operating of the BBCDR, as discussed in the JTF simulation.

The key variable *Flag* will be set to 1 when a bit error is detected ($\Delta\varphi_{\max} > \pi$). If *Flag* is equal to 0, $\varphi_{\text{in},p}$ increases by multiplying the factor Amp_step, and the bit-error-detection repeats until *Flag* $= 1$. It is worth mentioning that the iteration counter (j) is limited up to 20 for monitoring and avoiding the abnormal operation in the simulation. When the appropriate $\varphi_{\text{in},p}$is found, $\varphi_{in,p}$ *Sweep Loop* breaks in Fig. 14, and f_{jitter} is outputted with its corresponding $\varphi_{\text{in},p}$ as the JTOL value at a specific jitter frequency. Afterward, f_{jitter} changes to a lower frequency based on the f_{jitter} *Switch Algorithm*, which returns to the decision ($f_{\text{jitter}} > f_{\min}$). Then, we repeat the above procedure to obtain the overall JTOL curve. For example, we apply $\varphi_{\text{in}} = \varphi_{\text{in},p}\cdot\sin(2\pi \cdot 10^6 \cdot f_{\text{jitter}} \cdot t)$ and f_{jitter} is set to 80 MHz. $\varphi_{\text{in,p0}}$ is 0.4 UI and multiplied by Amp_step of 1.005 each time. The detection keeps operation until $\Delta\varphi_{\max} = \pi$. It can be found that when $\varphi_{in,p}$ reaches 0.5 UI, *Flag* $= 1$ is obtained. Next, f_{jitter} is reduced to

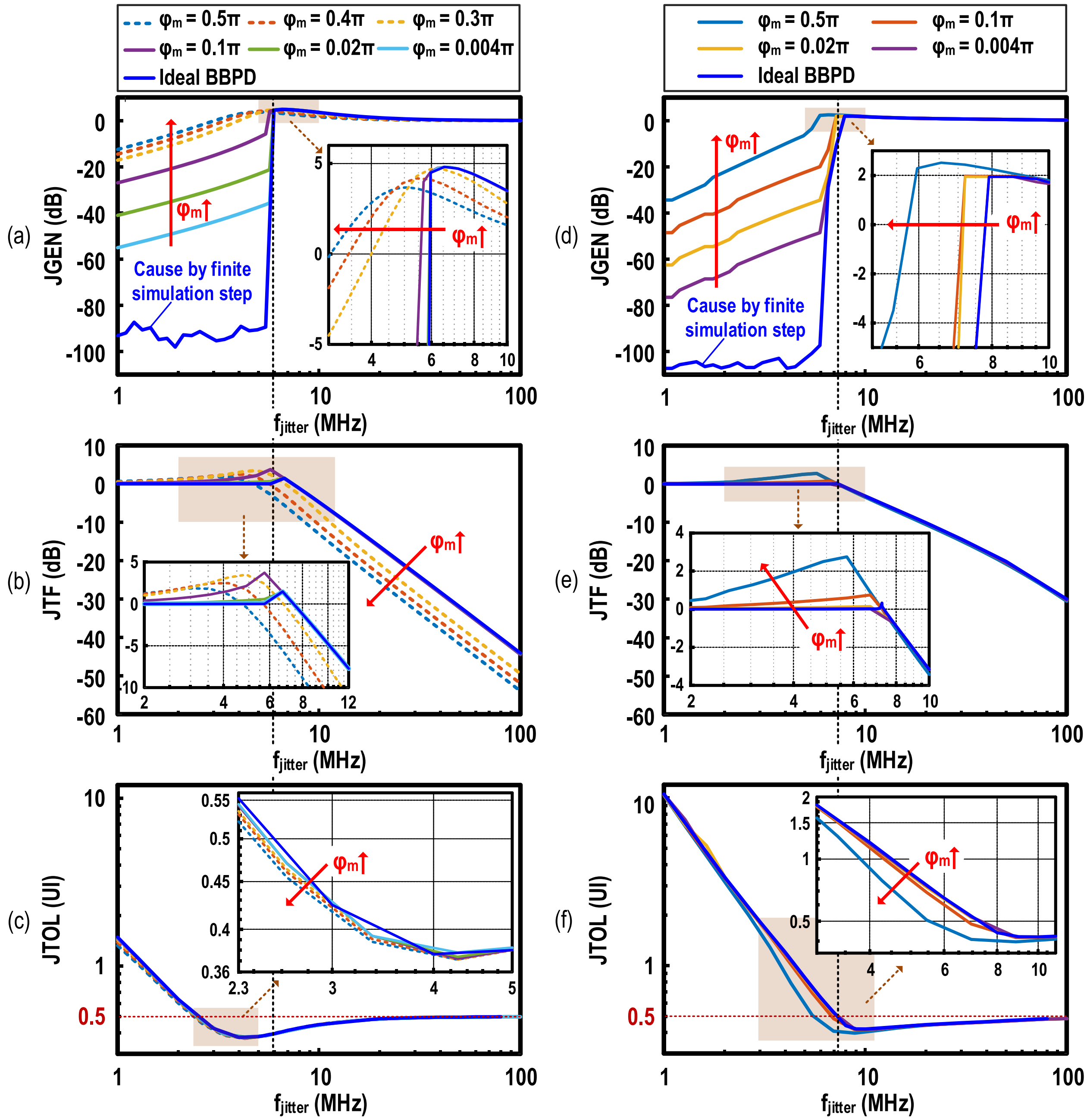

Fig. 19. Simulation results of JGEN (a) are obtained using the loop parameters LP-I in Table I with 0.1-UI $\varphi_{\mathrm{in},p}$ ($\varphi_{\mathrm{VCO},p}$), the corresponding JTF and JTOL are shown in (b) and (c). While the JGEN curves in (d) are obtained using the loop parameters LP-II in Table I with $k = 0.1$, the corresponding JTF and JTOL are shown in (e) and (f), respectively.

70 MHz. This procedure is repeated until f_{jitter} is less than f_{min} of 0.4 MHz. A group of $\varphi_{\mathrm{in},p}$ is achieved with their corresponding jitter frequencies. Finally, the overall JTOL curve is plotted by connecting $\varphi_{\mathrm{in},p}$ at 80, 70, 60 MHz and so on.

The simulation JTOL curves are obtained by performing the above algorithm, the AMP_step in the last run is set to 1.005, which guarantees the accuracy of the simulation. Fig. 15 shows the comparison of the simulation and calculation results according to (28), (29), and (32). Compared to the JTOL_3 based on the second-order LF (i.e., C_2 equals 0) from (32), JTOL_1 and JTOL_2 give better predictions, especially for the sinking area. Note that there is little difference between JTOL_1 and JTOL_2. Therefore, JTOL_2 is recommended for its simplicity. As depicted in Fig. 15, the calculated results predict the JTOL well at high frequency because the BBCDR experiences the full slewing all the time, which is consistent with the presupposition in Section IV. Inversely, at low f_{jitter}, the calculated JTOL_1 and JTOL_2 depart from the simulation results slightly, because the BBCDR operating at the specific frequency does not experience the full slewing any longer, as shown in Fig. 5(b). However, the theoretical curves from JTOL_1 and JTOL_2 are in high agreement with the simulation results.

Interestingly, the simulated JTOL curve of a third-order BBCDR exhibits a sinking area before approaching to 0.5 UI. It can be explained by the time-domain waveforms (Fig. 16). As f_{jitter} increases, φ_{out} presents a larger phase shift regarding φ_{in}, leading to a smaller Δt_2. Here, Δt_2 is the time difference between the minimum of φ_{in} and maximum of φ_{out}. Thus, $\Delta\varphi_{\max}$ increases even if the same $\varphi_{\text{in},p}$ is applied and the JTOL worsens. In the extreme case, when $\Delta t_2 = 0$, $\Delta\varphi_{\max} = \varphi_{\text{in},p} + \varphi_{\text{out},p}$, JTOL must be less than 0.5 UI, indicating a sinking point on the overall JTOL.

D. JGEN Simulation

For JGEN verification, a MATLAB/Simulink model [Fig. 17(a)] is developed according to the phase-domain behavior model in Fig. 3(b). φ_{in} is set to zero and an additive jitter is injected to the VCO by the subsystem φ_{VCO} *Generator*, which is the same as *Input Jitter Generator*in Fig. 9(a). The finite gain of the BBPD [26] is taken into account by the subsystem *Nonideal Binary Decision*, and its algorithm flowchart is shown in Fig. 17(b). When $-\varphi_m < \Delta\varphi < \varphi_m$, *BinaryOut* outputs $\Delta\varphi/\varphi_m$, indicating a finite gain. When $|\Delta\varphi| > \varphi_m$, it shows a binary characteristic, corresponding to the nonideal bang-bang curve (see Fig. 1).

Fig. 18(a) and (b) shows the simulated JGEN with a larger overshoot of 5 dB and JTF with a larger peak of 3 dB, respectively, under the loop parameters of LP-I with 0.1-UI $\varphi_{\text{VCO},p}(\varphi_{\text{in},p})$. Fig. 18(c) and (d) shows the simulated JGEN with a 2-dB overshoot and JTF with a 0.05-dB peak, respectively, using the loop parameters of LP-II with $k = 0.1$. For both loop parameters, we obtain the calculation results (dotted line) from (19) and (38), which is consistent with the simulation results (solid line) significantly. In addition, Fig. 18(a) and (c) shows the effect caused by the finite gain of the BBPD. For the ideal BBPD, JGEN exhibits an ideal high-pass characteristic, however, when φ_m increases, it shows a finite slope.

E. Overall Discussion Including the Effect of φ_m

Consider the above analysis, we must make the tradeoff between the insights from the calculation results and the calculation accuracy. Observing the deterioration of the BBPD curve by random jitter, we detail the effect of φ_m, ranging from 0 to 0.5π, in JGEN, JTF, and JTOL. Fig. 19(a)–(c) is obtained using the loop parameters of LP-I in Table I with 0.1-UI $\varphi_{\text{in},p}(\varphi_{\text{VCO},p})$ and Fig. 19(d)–(f) is achieved using the loop parameters of LP-II with $k = 0.1$. JGEN presents a typical high-pass profile, meaning that the BBCDR only suppresses low-frequency jitter of the VCO. For the ideal BBPD, a sharp rising appears at the corner frequency. Differing from the phenomenon when f_{jitter} is higher than the corner frequency, φ_1 follows φ_{VCO}, leading to $\varphi_{\text{out}} \approx 0$ at f_{jitter} lower than the corner frequency [Fig. 3(b)]. However, the discrete phase detection makes φ_{out} nonzero and random with $\varphi_{\text{out},p}$ in proportion to f_{VCO}. Thus, the curve in the well-tracked region is unsmooth and approximated as a constant. Meanwhile, the fast switching between well-tracked and slewing regions produces the sharp rising between them. As φ_m increases, the BBCDR loop attenuates less VCO jitter below the corner frequency. Finally, the behavior of a third-order linear CDR will occur when φ_m exceeds $\varphi_{\text{VCO},p}$.

For JTF in Fig. 19(b), if φ_m is larger than $\varphi_{\text{in},p}$ (e.g., 0.1 UI) and the BBPD completely operates in the linear phase-detection mode, JP decreases as φ_m increases (dashed line). JTF curves will be smooth without a sharp rising. Inversely, if φ_m is smaller than $\varphi_{\text{in},p}$ (e.g., 0.1 UI) and the BBPD fully enters the bang-bang phase-detection mode, JP increases as φ_m increases (solid line). This bang-bang phase-detection mode will hold in Fig. 19(e), when $\varphi_{\text{in},p}$ of 0.5 UI is relatively large compared to φ_m. JP is monotonically increasing with respect to φ_m, and thus the maximum JP occurs at $\varphi_m = 0.5$ UI [Fig. 19(e)]. The sinking region of JTOL is corresponding to the peaking area of JGEN and JTF. Moreover, the corner frequency moves to lower frequency slightly with lower magnitude of JTOL.

VII. Conclusion

The JTF, JTOL, and JGEN characteristics of the third-order BBCDR have been studied in terms of LG, indicating that they share the same corner frequencies. The time-domain waveforms happening in the well-tracked region and slewing region in the vicinity of the corner frequency have been analyzed. The leveraged insights explain the sinking area of JTOL and the sharp rising of JGEN. The resultant formulas confirm the C_2 contribution to the BBCDR loop design when compared with the conventional analysis of a second-order BBCDR loop. The MATLAB/Simulink models are developed to verify the accuracy of our analytical methods. Meanwhile, in order to match a practical condition, the nonideal effect of BBPD has been discussed in the simulation results. This paper focuses on the analysis of the full-rate third-order BBCDR loop, indicating its effectiveness and practicability for analyzing the features of the half-rate and quarter-rate BBCDR with the different frequencies of the VCO. When the divider in the feedback path can be taken into consideration in the phase-domain behavior model, the analytical method and conclusion can be modified to reveal the characteristics of the bang-bang PLL.

References

[1] B. Razavi, "Challenges in the design high-speed clock and data recovery circuits," *IEEE Commun. Mag.*, vol. 40, no. 8, pp. 94–101, Aug. 2002.

[2] M. Talegaonkar, R. Inti, and P. K. Hanumolu, "Digital clock and data recovery circuit design: Challenges and tradeoffs," in *Proc. IEEE Custom Integr. Circuits Conf. (CICC)*, Sep. 2011, pp. 1–8.

[3] J. Jin, S. Kim, X. Jin, S.-H. Kim, and J.-H. Chun, "A 12.5-Gb/s near-ground transceiver employing a maxeye algorithm-based adaptation technique," *IEEE Trans. Very Large Scale Integr. (VLSI) Syst.*, vol. 26, no. 3, pp. 522–530, Mar. 2018.

[4] J. Han, H. Won, and H.-M. Bae, "0.6–2.7-Gb/s referenceless parallel CDR with a stochastic dispersion-tolerant frequency acquisition technique," *IEEE Trans. Very Large Scale Integr. (VLSI) Syst.*, vol. 22, no. 6, pp. 1219–1225, Jun. 2014.

[5] J. Lee *et al.*, "A 4 × 10-Gb/s referenceless-and-masterless phase rotator-based parallel transceiver in 90-nm CMOS," *IEEE Trans. Very Large Scale Integr. (VLSI) Syst.*, vol. 24, no. 6, pp. 2310–2320, Jun. 2016.

[6] C. Gimeno, D. Bol, and D. Flandre, "Multilevel half-rate phase detector for clock and data recovery circuits," *IEEE Trans. Very Large Scale Integr. (VLSI) Syst.*, vol. 26, no. 9, pp. 1807–1811, Sep. 2018.

[7] J. Savoj and B. Razavi, "A 10-Gb/s CMOS clock and data recovery circuit with a half-rate linear phase detector," *IEEE J. Solid-State Circuits*, vol. 36, no. 5, pp. 761–768, May 2001.

[8] I. Jung, D. Shin, T. Kim, and C. Kim, "A 140 Mb/s to 1.96 Gb/s referenceless transceiver with 7.2 μs frequency acquisition time," *IEEE Trans. Very Large Scale Integr. (VLSI) Syst.*, vol. 19, no. 7, pp. 1310–1315, Jul. 2011.

[9] F. Centurelli *et al.*, "A 10-Gb/s CMU/CDR chip-set in SiGe BiCMOS commercial technology with multistandard capability," *IEEE Trans. Very Large Scale Integr. (VLSI) Syst.*, vol. 13, no. 2, pp. 191–200, Feb. 2005.

[10] J. Song, S. Hwang, and C. Kim, "A 4 × 5-Gb/s 1.12-μs slocking time reference-less receiver with asynchronous sampling-based frequency acquisition and clock shared subchannels," *IEEE Trans. Very Large Scale Integr. (VLSI) Syst.*, vol. 24, no. 8, pp. 2768–2777, Aug. 2016.

[11] M. Verbeke *et al.*, "A 1.8-pJ/b, 12.5–25-Gb/s wide range all-digital clock and data recovery circuit," *IEEE J. Solid-State Circuits*, vol. 53, no. 2, pp. 470–483, Feb. 2018.

[12] T. Lee, Y.-H. Kim, J. Sim, J.-S. Park, and L.-S. Kim, "A 5-Gb/s 2.67-mW/Gb/s digital clock and data recovery with hybrid dithering using a time-dithered delta–sigma modulator," *IEEE Trans. Very Large Scale Integr. (VLSI) Syst.*, vol. 24, no. 4, pp. 1450–1459, Apr. 2016.

[13] G. Wu *et al.*, "A 1–16 Gb/s all-digital clock and data recovery with a wideband high-linearity phase interpolator," *IEEE Trans. Very Large Scale Integr. (VLSI) Syst.*, vol. 24, no. 7, pp. 2511–2520, Jul. 2016.

[14] T. Lee, Y.-H. Kim, and L.-S. Kim, "A 5-Gb/s digital clock and data recovery circuit with reduced DCO supply noise sensitivity utilizing coupling network," *IEEE Trans. Very Large Scale Integr. (VLSI) Syst.*, vol. 25, no. 1, pp. 380–384, Jan. 2017.

[15] J.-M. Lin, C.-Y. Yang, and H.-M. Wu, "A 2.5-Gb/s dll-based burst-mode clock and data recovery circuit with 4× oversampling," *IEEE Trans. Very Large Scale Integr. (VLSI) Syst.*, vol. 23, no. 4, pp. 791–795, Apr. 2015.

[16] R. Navid *et al.*, "A 40 Gb/s serial link transceiver in 28 nm CMOS technology," *IEEE J. Solid-State Circuits*, vol. 50, no. 4, pp. 814–827, Apr. 2015.

[17] N. D. Dalt, "Markov chains-based derivation of the phase detector gain in bang-bang PLLs," *IEEE Trans. Circuits Syst. II, Exp. Briefs*, vol. 53, no. 11, pp. 1195–1199, Nov. 2006.

[18] B. Chun and M. P. Kennedy, "Statistical properties of first-order bang-bang PLL with nonzero loop delay," *IEEE Trans. Circuits Syst. II, Exp. Briefs*, vol. 55, no. 10, pp. 1016–1020, Oct. 2008.

[19] S. Tertinek, J. P. Gleeson, and O. Feely, "Statistical analysis of first-order bang-bang phase-locked loops using sign-dependent random-walk theory," *IEEE Trans. Circuits Syst. I, Reg. Papers*, vol. 57, no. 9, pp. 2367–2380, Sep. 2010.

[20] S. Tertinek and O. Feely, "Investigation of first-order digital bang-bang phase-locked loops with reference clock jitter," in *Proc. NORCHIP*, Nov. 2008, pp. 217–222.

[21] F. A. Musa and A. C. Carusone, "Modeling and design of multilevel bang–bang CDRs in the presence of ISI and noise," *IEEE Trans. Circuits Syst. I, Reg. Papers*, vol. 54, no. 10, pp. 2137–2147, Oct. 2007.

[22] R. C. Walker, "Designing bang-bang PLLs for clock and data recovery in serial data transmission systems," in *Phase-locking in High Performance Systems*, B. Razavi, Ed. Piscataway, NJ, USA: IEEE Press, 2003, pp. 34–45.

[23] M. van Ierssel, H. Yamaguchi, A. Sheikholeslami, H. Tamura, and W. W. Walker, "Event-driven modeling of CDR jitter induced by power-supply noise, finite decision-circuit bandwidth, and channel ISI," *IEEE Trans. Circuits Syst. I, Reg. Papers*, vol. 55, no. 5, pp. 1306–1315, Jun. 2008.

[24] C. He and T. Kwasniewski, "Bang-bang CDR's acquisition, locking, and jitter tolerance," in *Proc. 25th IEEE Can. Conf. Elect. Comput. Eng. (CCECE)*, May 2012, pp. 1–4.

[25] J. Lee, K. S. Kundert, and B. Razavi, "Analysis and modeling of bang-bang clock and data recovery circuits," *IEEE J. Solid-State Circuits*, vol. 39, no. 9, pp. 1571–1580, Sep. 2004.

[26] H. Adrang and H. Miar-Naimi, "Modeling of jitter in bang-bang CDR with Fourier series analysis," *IEEE Trans. Circuits Syst. I, Reg. Papers*, vol. 60, no. 1, pp. 3–10, Jan. 2013.

[27] S. Cheng, H. Tong, J. Silva-Martinez, and A. L. Karslayan, "Steady-state analysis of phase-locked loops using binary phase detector," *IEEE Trans. Circuits Syst. II, Exp. Briefs*, vol. 54, no. 6, pp. 474–478, Jun. 2007.

[28] J. D. H. Alexander, "Clock recovery from random binary signals," *Electron. Lett.*, vol. 11, no. 22, pp. 541–542, Oct. 1975.

Xinyi Ge received the B.Eng. degree in electronic science and technology from the University of Electronic Science and Technology of China, Chengdu, China, in 2016. He is currently working toward the M.S. degree at the State-Key Laboratory of Analog and Mixed-Signal VLSI (AMSV), University of Macau, Macau, China.

His current research interests include high-speed clock and data recovery (CDR) design.

Yong Chen (S'10–M'11) received the B.Eng. degree in electronic and information engineering from the Communication University of China (CUC), Beijing, China, in 2005, and the Ph.D. degree in microelectronics and solid-state electronics from the Institute of Microelectronics of Chinese Academy of Sciences (IMECAS), Beijing, in 2010.

He is currently an Assistant Professor at the State-Key Laboratory of Analog and Mixed-Signal VLSI (AMSV) and the Institute of Microelectronics (IME), University of Macau, Macau, China. He is involved in IC design comprising analog/RF/mm-wave/wireline. He reports two chip inventions at the 2019 IEEE International Solid-State Circuits Conference—ISSCC (Chip Olympics): mm-wave phase-locked loop (PLL) (2019) and voltage-controlled oscillator (VCO) (2019).

Xiaoteng Zhao (S'18) received the B.Eng. degree in integrated circuit design and integration system from XiDian University, Shaanxi, China, in 2014, and the M.Eng. degree in integrated circuit engineering from the University of Chinese Academy of Sciences, Beijing, China, in 2017. He is currently working toward the Ph.D. degree at the State-Key Laboratory of Analog and Mixed-Signal VLSI (AMSV), University of Macau, Macau, China.

His current research interests include the high-speed wireline backplane transceiver design.

Pui-In Mak (S'00–M'08–SM'11–F'19) received the Ph.D. degree from the University of Macau (UM), Macao, China, in 2006.

He is currently a Full Professor at the Department of Electrical and Computer Engineering, Faculty of Science and Technology, UM, and an Associate Director (Research) at the State-Key Laboratory of Analog and Mixed-Signal VLSI, UM. His current research interests include analog and radio frequency (RF) circuits and systems for wireless and multidisciplinary innovations.

Dr. Mak was a member of Board-of-Governors of IEEE Circuits and Systems Society from 2009 to 2011 and as an Editorial Board Member of IEEE Press from 2014 to 2016. He was a co-recipient of the DAC/ISSCC Student Paper Award'05, the CASS Outstanding Young Author Award'10, the National Scientific and Technological Progress Award'11, the Best Associate Editor of the IEEE TRANSACTIONS ON CIRCUITS AND SYSTEMS—Part II: EXPRESS BRIEFS from 2012 to 2013, the A-SSCC Distinguished Design Award'15, and the ISSCC Silkroad Award'16. He was a recipient of the Honorary Title of Value for scientific merits by the Macau Government in 2005. He is/was the TPC Vice Co-Chair of ASP-DAC in 2016, a TPC Member of A-SSCC from 2013 to 2016. He has been with ESSCIRC and ISSCC since 2016. He is/was Distinguished Lecturer of the IEEE Circuits and Systems Society from 2014 to 2015 and the IEEE Solid-State Circuits Society from 2017 to 2018. He served as a Senior Editor of the IEEE JOURNAL ON EMERGING AND SELECTED TOPICS IN CIRCUITS AND SYSTEMS from 2014 to 2015, a Guest Editor of the IEEE RFIC VIRTUAL JOURNAL in 2014 and the IEEE JOURNAL OF SOLID-STATE CIRCUITS in 2018, an Associate Editor of the IEEE TRANSACTIONS ON CIRCUITS AND SYSTEMS—Part I: Regular Papers from 2010 to 2011 and from 2014 to 2015, and the IEEE TRANSACTIONS ON CIRCUITS AND SYSTEMS—Part II: EXPRESS BRIEFS from 2010 to 2013.

Rui P. Martins (M'88–SM'99–F'08) was born in 1957. He received the bachelor's (5-years), master's, Ph.D. degrees, and the Habilitation degree for Full-Professor in electrical engineering and computers from the Department of Electrical and Computer Engineering, Instituto Superior Técnico (IST), Technical University of Lisbon (TU Lisbon), Lisbon, Portugal, in 1980, 1985, 1992, and 2001, respectively.

Since 1980, he has been with the Department of Electrical and Computer Engineering (DECE)/IST, TU Lisbon. Since 1992, he has been on leave from IST, TU Lisbon. From 1994 to 1997, he was the Dean of the Faculty, Faculty of Science and Technology (FST), University of Macau (UM), Macau, China, where he has been the Vice-Rector since 1997. Since 2008, after the reform of the UM Charter, he was nominated after open international recruitment, and reappointed in 2013, as a Vice Rector (Research) until 2018. From 2001 to 2002, he served as a Co-Founder of Synopsys, Macau. In 2003, he established the Analog and Mixed-Signal VLSI Research Laboratory, UM. In 2011, he became the Founding Director of the State-Key Laboratory of China (the first in Engineering), Macau. Within the scope of his teaching and research activities, he has taught 21 bachelor and master courses. He has supervised (or co-supervised) 40 theses (19 Ph.D. and 21 master's) in UM. He is currently with the Department of Electrical and Computer Engineering, FST, UM, where he has been the Chair-Professor since 2013. He has coauthored 6 books and 9 book chapters, 377 papers in scientific journals (111) and in conference proceedings (266), and 60 other academic works, in a total of 470 publications. He holds 18 patents (16 USA and 2 Taiwan).

Dr. Martins was a member of the IEEE CASS Fellow Evaluation Committee in 2013 and 2014 and the Circuits and Systems (CAS) Society Representative in the Nominating Committee, for the election in 2014, of the Division I (CASS/EDS/SSCS)—the Director of the IEEE. He was a recipient of the nomination of the Best Associate Editor of the IEEE TRANSACTIONS ON CIRCUITS AND SYSTEMS—Part II: EXPRESS BRIEFS from 2012 to 2013 and two government decorations, the Medal of Professional Merit from Macao Government (Portuguese Administration) in 1999 and the Honorary Title of Value from Macao SAR Government (Chinese Administration) in 2001. He served as the Founding Chairman for both IEEE Macau Section from 2003 to 2005 and the IEEE Macau Joint-Chapter on CAS/Communications (COM) from 2005 to 2008 [2009 World Chapter of the Year of IEEE CAS Society (CASS)]. In 2010, he was elected, unanimously, as a Corresponding Member of the Portuguese Academy of Sciences, Lisbon, being the only Portuguese Academician living in Asia. He was the General Chair of the 2008 IEEE Asia–Pacific Conference on CAS (APCCAS'2008) and the Vice-President for Region 10 (Asia, Australia, and the Pacific) of IEEE CASS from 2009 to 2011. Since 2011, he has been the Vice-President (World) Regional Activities and Membership of IEEE CASS from 2012 to 2013. He was the General Chair of the ACM/IEEE Asia South Pacific Design Automation Conference—ASP-DAC'2016. He was a Nominations Committee Member of IEEE CASS in 2016. He is the Chair of the IEEE Fellow Evaluation Committee class of 2018 of IEEE CASS. He was an Associate Editor of the IEEE TRANSACTIONS ON CIRCUITS AND SYSTEMS—Part II: EXPRESS BRIEFS from 2010 to 2013.